

Full Length Article

Analysis of flame instability in low-emission tower-type gas turbine combustor with multi-stage methane injection

Enhui Liu^{a,b}, Jinghe Lu^{a,b}, Chenyang Cao^b, Xiao Liu^{a,*}, Hongtao Zheng^a, Huangwei Zhang^{b,*}

^a College of Power and Energy Engineering, Harbin Engineering University, Harbin 150001, China

^b Department of Mechanical Engineering, National University of Singapore, 9 Engineering Drive 1, Singapore 117576, Singapore



ARTICLE INFO

Keywords:

Large eddy simulation
Lean-premixed combustion
Model gas turbine combustor
Multi-stage fuel injection
Combustion instability
Flashback

ABSTRACT

A low-emission tower-type coaxial-staged combustor with a pilot stage, first main stage and second main stage is simulated in this study. The flow field, flame structure, vortex-mixing interaction, and flame instabilities are predicted with large eddy simulation and partially stirred reactor model. Heat radiation is not considered in the simulations. The results show that the maximum of the averaged length and width of the inner recirculation zone are approximately 249.8 and 71.3 mm, respectively. The distributions of the fuel from various stages in the combustor are analyzed based on the respective mixture fractions. The pressure and heat release rate (HRR) in the combustor fluctuate periodically with a frequency of about 373 Hz. Both HRR and pressure fluctuations increase and then decrease with time, and there is a phase difference of 46.1° between them. Due to the combustion instabilities, the flame structures change periodically, including attached flame and lifted V-shaped flame, in one HRR oscillation cycle. Moreover, the swirling flame length also varies periodically with time. As the pilot stage and first main stages are turned-off, the frequency of HRR fluctuations and pressure fluctuations, as well as the flame root dynamics, are significantly affected. It is also found that the effects of the fuel ratio of the first and second main stages have a significant influence on the flame root dynamics, e.g., different degrees of flashback observed in different cases.

1. Introduction

With increasingly stringent environmental regulations, low-emission combustion technologies are in high demand [1,2]. Lean-premixed combustion is an effective method to reduce nitrogen oxide (NO_x) emissions [3,4]. Nonetheless, it is prone to thermoacoustic oscillation [5–7], flashback [8,9], and local quenching [10]. Therefore, understanding the unsteady flame behaviors are critical to develop or optimize low-emission combustor technologies.

There have been numerous studies on flow and flame dynamics in model gas turbine combustors, in terms of fuel–air mixing, flame structure, and combustion instability. Stöhr [11] et al., for instance, visualized the fuel–air mixing by acetone-PLIF, and found that the vortex-induced mixing facilitates flame stabilization. They also concluded that the fuel–air mixing by a precessing vortex core (PVC) plays a significant role in stabilizing the flame. Moreover, Stöhr et al. [12] and Litvinov et al. [13] also mentioned the effects of the PVC on flame structure and mixing. They observed the effects of double helical vortex (DHV) in the outer shear layer (OSL). The DHV causes a regular

sequence of flame roll-up, mixing of burned and unburned gases, and subsequent ignition of the mixture in the OSL. Moreover, Chen et al. [14] found the mixing of the fuel and air are consumed in the shear layer between the IRZ and mainstream in a stable flame. However, in an unstable flame, the periodic variations of air mass flow rate would result in a periodic radial flapping of the fuel jets.

Combustion instability in various configuration of gas-turbine-like flames is also widely investigated. For instance, Zhang et al. [15] explored the effects of swirl number on thermoacoustic instabilities in a lean premixed swirl combustor. They found that the combustor is stable when the swirl numbers are under 0.5. A transition from stable state to thermoacoustic instabilities occurs when the swirler number is 0.5 – 0.6. Also, Meier et al. [16] found that both the flow field and flame shape are different between non-pulsating and pulsating flames. Based on their measurements, combustion instability or pulsation at a frequency of around 290 Hz happens in the pulsating flame, and the fluctuations of pressure and heat release rate are in phase. The variations of CH₄ in these flames results in different unmixedness of fuel and air, which further influences the flame and the heat release rate. Fredrich et al. [17]

* Corresponding authors.

E-mail addresses: liuxiao_heu@163.com (X. Liu), huangwei.zhang@nus.edu.sg (H. Zhang).

studied the combustion instability mechanism in a gas turbine model combustor. Periodic pressure fluctuations at a frequency of 300 Hz in the air plenum and combustion chamber cause the fluctuating flow rate for the chamber. Meanwhile, fuel accumulation inside the swirler would also lead to local equivalence ratio variations. These two effects increase the unsteadiness of heat release, which induces combustion instability. Also, the fluctuating heat release rate and pressure with the growth rates equal to zero show a thermo-acoustic limit-period oscillation in the combustion. Temme et al. [18] also found that the equivalence ratio oscillation in the partially premixed mode is the main driving mechanism of thermoacoustic instabilities. Wang et al. [19] studied the flame structures and thermoacoustic instabilities in a centrally staged swirl burner with varying stratification ratios and partially premixed modes. With increased stratification ratio, the flame structure starts to change. They also found that the partial premixing in the main stage excites stronger thermoacoustic instabilities and thus leads to different flame structures. Chen et al. [20] found that stagnation points of the PVC provide an anchoring mechanism in both stable and unstable flames, while the PVC is stretched and compressed by flame oscillations, and the pressure fluctuations is at a frequency of about 300 Hz. Agostinelli et al. [21] found a weak 480 Hz peak by the pressure signal spectrum in the simulation of the unstable flame. A frequency of 392 Hz is the dominant thermo-acoustic in the study by Arndt et al. [22].

Despite the foregoing encouraging results on the mixing of flow field, flame structures and combustion instability, limited studies are focused on the effects of fuel mass flow rate from various injection stages on flame dynamics and combustion stability in a multi-stage swirler. The present paper addresses the above said effects in a low-emission tower-type coaxial-staged combustor (LETCC) fueled with methane. In our work, the fuels from pilot stage and/or first main stage are turned-off to compare the impacts of each stage. Moreover, different fuel ratios of first main stage and the second main stage are also investigated. The rest of the paper is organized as follows. The mathematical models are presented in Section 2, whilst section 3 introduces the experimental configuration. Section 4 gives detailed numerical information, including operating conditions and mesh resolution. In Section 5, the results are presented and discussed. The main conclusions are summarized in Section 6.

2. Mathematical model

2.1. LES equation

The filtered equations of mass, momentum, energy, and species mass fraction read [23]

$$\frac{\partial \bar{\rho}}{\partial t} + \frac{\partial (\bar{\rho} \tilde{u}_i)}{\partial x_i} = 0 \quad (1)$$

$$\frac{\partial (\bar{\rho} \tilde{u}_i)}{\partial t} + \frac{\partial (\bar{\rho} \tilde{u}_i \tilde{u}_j)}{\partial x_j} = - \frac{\partial \bar{p}}{\partial x_i} + \frac{\partial [\bar{\rho} (\bar{\tau}_{ij} - \tau_{ij}^{\text{sgs}})]}{\partial x_j} \quad (2)$$

$$\begin{aligned} \frac{\partial (\bar{\rho} \tilde{h}_s)}{\partial t} + \frac{\partial (\bar{\rho} \tilde{u}_i \tilde{h}_s)}{\partial x_i} = & - \partial [\bar{\rho} (\tilde{u}_i \tilde{h}_s - \tilde{u}_i \tilde{h}_s)] \\ & \partial x_i + \frac{\partial}{\partial x_i} \left(\frac{\mu}{Pr} \frac{\partial \bar{T}}{\partial x_i} \right) + \frac{\partial \bar{p}}{\partial t} + \tilde{u}_i \frac{\partial \bar{p}}{\partial x_i} + \bar{\omega}_T \end{aligned} \quad (3)$$

$$\begin{aligned} \frac{\partial (\bar{\rho} \tilde{Y}_k)}{\partial t} + \frac{\partial (\bar{\rho} \tilde{u}_i \tilde{Y}_k)}{\partial x_i} = & - \partial [\bar{\rho} (\tilde{u}_j \tilde{Y}_k - \tilde{u}_j \tilde{Y}_k)] \\ & \partial x_i + \frac{\partial}{\partial x_i} \left(\frac{\mu}{Sc} \frac{\partial \tilde{Y}_k}{\partial x_i} \right) + \bar{\omega}_k \end{aligned} \quad (4)$$

t is time, $x_{i(i=1,2,3)}$ the i -th spatial coordinate, and $u_{i(i=1,2,3)}$ the velocity components in the i -th direction. $\bar{\rho}$ and \bar{p} are the filtered density and pressure, respectively. $\bar{\tau}_{ij}$ is the filtered viscous stress tensor. \tilde{h}_s is the

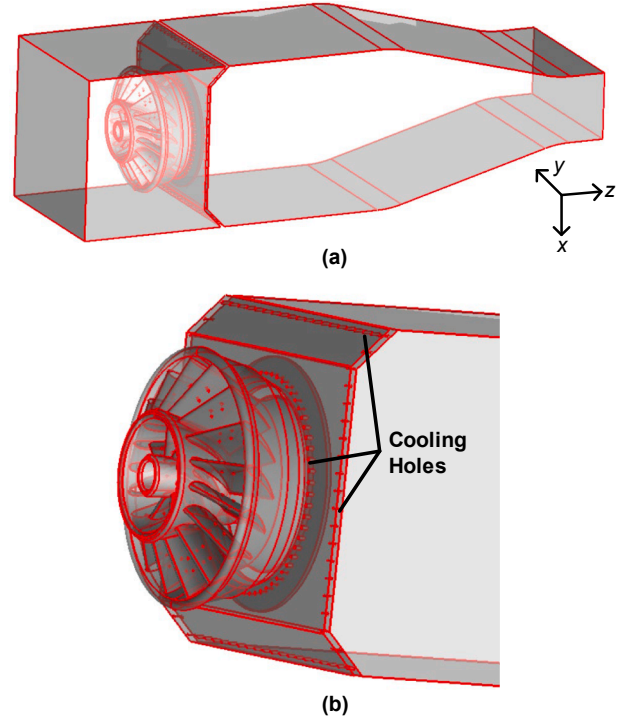


Fig. 1. A schematic of a tower-type coaxial-staged combustor.

filtered sensible enthalpy, $\tilde{u}_i \tilde{h}_s - \tilde{u}_i \tilde{h}_s$ the enthalpy fluxes, μ the dynamic viscosity, and $\bar{\omega}_T$ the heat release rate. Sc and Pr are the Schmidt and Prandtl numbers, respectively. \tilde{Y}_k is the mass fraction of the k -th species, and $\tilde{u}_j \tilde{Y}_k - \tilde{u}_j \tilde{Y}_k$ is the k -th species mass flux. The reaction source term $\bar{\omega}_k$ is estimated with a sub-grid scale (SGS) combustion model, which will be detailed in Section 2.2.

The SGS stress tensor τ_{ij}^{sgs} from Eq. (2) reads

$$\tau_{ij}^{\text{sgs}} = \tilde{u}_i \tilde{u}_j - \tilde{u}_i \tilde{u}_j = \frac{1}{3} \delta_{ij} \tau_{kk} + 2\nu_{\text{sgs}} \bar{S}_{ij} \quad (5)$$

in which δ_{ij} is the Kronecker delta function. \bar{S}_{ij} is the resolved strain rate tensor

$$\bar{S}_{ij} = \frac{1}{2} \left(\frac{\partial \tilde{u}_i}{\partial x_j} + \frac{\partial \tilde{u}_j}{\partial x_i} \right) \quad (6)$$

ν_{sgs} is the SGS viscosity. The SGS stress tensor is modelled with the wall-adapting local eddy-viscosity (WALE) model [24].

2.2. Combustion model

The partially stirred reactor (PaSR) model [25] is used to predict the resolved chemical reaction rates in LES and this model has been widely adopted in previous studies, e.g., [26–29]. In the PaSR model, the computational cell is divided into two parts, i.e., a reacting zone and a non-reacting zone. The reaction rate can be calculated from [30]

$$\bar{\omega}_k = \bar{\omega}(\bar{\rho}, Y_k, T) = \frac{\tau_c}{\tau_c + \tau_m} \bullet \bar{\omega}(\tilde{\rho}, \tilde{Y}_k, \tilde{T}) \quad (7)$$

where τ_c and τ_m are the chemical reaction and turbulent mixing time-scales, respectively. The chemical reaction timescale τ_c is estimated from the laminar flame speed s_u at the laminar flame thickness $\delta_{u,l}$, i.e., $\tau_c \approx \delta_{u,l}/s_u$ [31]. The turbulent mixing timescale τ_m is calculated from

$$\tau_m = 0.5 \sqrt{\tau_{\Delta} \tau_k} \quad (8)$$

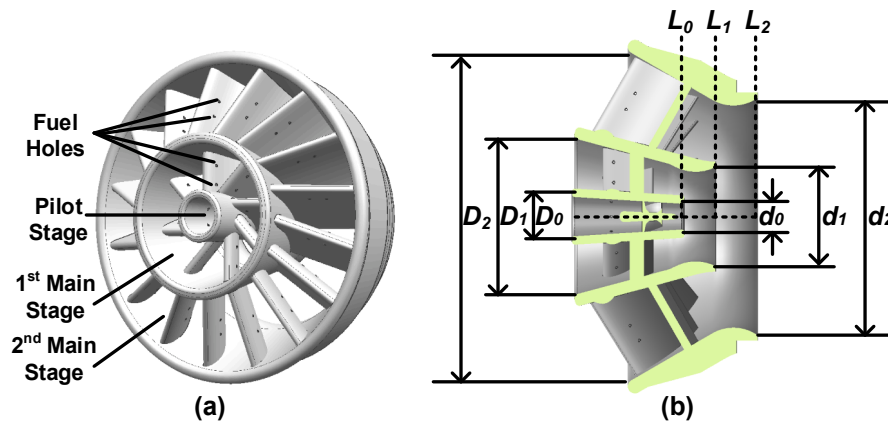


Fig. 2. (a) Structure of the swirler and (b) the diameter and exit location of the swirler. The subscripts of 0, 1, and 2 present the pilot stage, the first main stage and second main stage, respectively. L_i indicates the exit locations of different stages.

Table 1
Geometrical parameters of the swirler.

D_0 [mm]	D_1 [mm]	D_2 [mm]	d_0 [mm]	d_1 [mm]	d_2 [mm]
16	55	116	9	35	82

where $\tau_\Delta = \Delta/\sqrt{2k/3}$ is the sub-grid scale timescale, $\tau_k = (\nu/\varepsilon)^{1/2}$ the Kolmogorov time scale, k the SGS kinetic energy, ν the laminar kinematic viscosity, and ε the dissipation rate.

3. Experimental configuration

A schematic of tower-type coaxial-staged combustor is shown in Fig. 1(a). Dry air enters a square plenum (165 mm × 165 mm) and flows into the combustor along two directions. Majority of the air passes the swirlers and enters the combustor, whilst the rest enters the combustor through the cooling holes, as annotated in Fig. 1(b). There are three stages of the swirler system, including one pilot stage and two main stages, as marked in Fig. 2(a). The multi-stage system is designed for achieving low NO_x and stable combustion. The air passes the pilot stage and the first main stage along the axial direction. The air in the second main stage enters the swirler in an oblique radial manner, which is termed as *tower swirler*. The fuel is pure methane, and the injectors with a diameter of 1 mm, they are located on the blade sides in two main stages and hub in the pilot stage, as illustrated in Fig. 2(a). The total numbers of the fuel injectors in the pilot stage, the first main stage and second main stage are 6, 32 and 64, respectively.

The details of the swirlers are demonstrated in Fig. 2(b) and their geometrical parameters are listed in Table 1. D_i and d_i are the diameters of the inlet and outlet. In this study, the blade angle is 50° for the two main stages and 45° for the pilot stage. Based on the velocity profiles at the exit of each main stage, the swirl number, S , is calculated as the ratio between the tangential and axial momentum fluxes [12,32], i.e.,

$$S = \frac{\int_0^R \rho u v 2\pi r^2 dr}{(R \int_0^R \rho u^2 2\pi r dr)} \quad (9)$$

Based on Eq. (9), the swirl number are 0.65, 0.7 and 0.83 for the pilot stage, the first and second main stages, respectively.

4. Numerical implementation

4.1. Numerical method

The LES is performed on the ASPIRE 1 Cluster from National Supercomputer Centre in Singapore using 720 cores, and the governing

Table 2

Fuel and air conditions. M_{air} and M_{CH_4} are the total mass flow rates of air and CH₄ respectively, T_{air} and T_{CH_4} are the air temperature of air and CH₄, ϕ equivalence ratio, and p pressure.

M_{air} [kg/s]	0.17	M_{CH_4} [kg/s]	0.0052
T_{air} [K]	600	T_{CH_4} [K]	300
ϕ [-]	0.55	p [MPa]	0.1

Table 3

Information of case 0–4. $M_{CH_4-pilot}$, M_{CH_4-1st} and M_{CH_4-2nd} are the fuel mass flow rates in the pilot, first and second main stages. Φ_{1st} and Φ_{2nd} are the equivalence ratio of the first and second main stages. $R_\phi = \Phi_{1st}/\Phi_{2nd}$ and $R_M = M_{CH_4-1st}/M_{CH_4-2nd}$.

Case	R_ϕ	R_M	$M_{CH_4-pilot}$ [g/s]	M_{CH_4-1st} [g/s]	M_{CH_4-2nd} [g/s]
0	1:1	1:5.7	0.0921	0.75	4.36
1	1:1	1:5.7	0.0921	0.75	4.36
2	1:1	1:5.7	0	0.76	4.44
3	0	0	0	0	5.2
4	5.7:1	1:1	0.0921	2.55	2.55

equations are solved with OpenFOAM 6.0 [33]. The detailed mechanism for methane combustion, GRI 3.0 [34], is adopted, which has 53 species and 325 elementary reactions. The PIMPLE algorithm [35] is applied to solve the pressure–velocity coupling. The unsteady terms are discretized by a first-order Euler scheme and the time step is 10^{-6} s. The linear-upwind stabilized transport scheme is used for the convection terms in the momentum equations, whilst the total variation diminishing scheme for the convection terms in the energy and species equations. The central differencing is used for the diffusion terms in Eqs. (2)–(4).

To increase the computational efficiency (or save the computational time) when detailed chemistry is considered, the Tabulation of Dynamic Adaptive Chemistry (TDAC) method, which combined in-situ adaptive tabulation (ISAT) and dynamic adaptive chemistry (DAC) reduction, is used in this work. The IAST [36,37] is a tabulation method and aims to reuse the previously computed results to decrease the effect of the number of cells. Moreover, the DAC [38] is an on-the-fly mechanism reduction method to reduce the mechanism size. The search initiating species include CH₄, CO, and HO₂. These species play primary roles in the fuel decomposition, CO oxidation, and H₂ reactions. The tolerances for the DAC and ISAT are 10^{-3} and 10^{-4} , respectively [39].

4.2. Simulation case

The operating conditions of the tower-type coaxial-staged combustor

Table 4

Fuel initial velocity in case 0–4. V_{pilot} , V_{1st} and V_{2nd} are the velocity of pilot stage, the first main stage and the second main stage, respectively.

Case	V_{pilot} [m/s]	V_{1st} [m/s]	V_{2nd} [m/s]
0	30.35	46.60	134.51
1	30.35	46.60	134.51
2	0	47.4	136.94
3	0	0	160.66
4	30.35	157.8	78.90

are tabulated in Table 2. The total mass flow rate of the air is 0.17 kg/s, whereas the air through the cooling holes accounts for about 5% by mass, the cooling air is not considered in the estimation of the global equivalence ratio (ϕ) in Table 2. In this paper, we will investigate four cases, considering various methane mass flow rates in each stage. Their details are given in Table 3. Cases 0 and 1 have the same conditions, but

they respectively consider nonreacting and reacting flows. Case 1 is deemed the baseline case for flame simulations, in which the methane is injected from all stages. As seen from Table 3, the ratio of the mass flow rates of two main stages is 1:1. The fuel percentages from the pilot, first, and second main stages are 0.0921, 0.75 and 4.36 g/s, respectively. The air percentages from the pilot, first, and second main stages are 0.026, 0.238, 1.37 kg/s. To reduce the NOx, the equivalence ratio of the pilot stage is designed as 0.6, so the fuel of the pilot stage is 0.0921 g/s. The equivalence ratio of the first and second main stage is 1:1, and the fuel flow rates of the first and second stage are 0.75 and 4.36 g/s, respectively. In case 2, the pilot fuel is switched off, with the main stage conditions identical to those in case 1. Comparisons between case 1 and 2 would reveal the influences of pilot fuel injection on flame dynamics. Moreover, in case 3, both fuels from the pilot and first main stages are deactivated, and comparisons between case 1–3 can illustrate the effects of the first main stage. Furthermore, case 1 and 4 aim to explore the

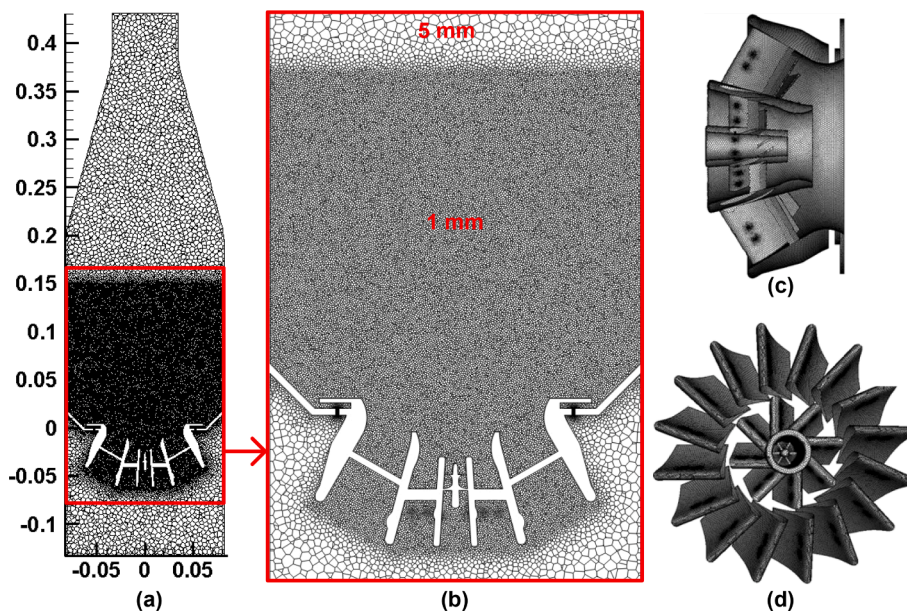


Fig. 3. (a) CFD mesh distribution at $y = 0$ plane, (b) local mesh refinement area, (c) surface meshes of the swirler, and (d) the blade.

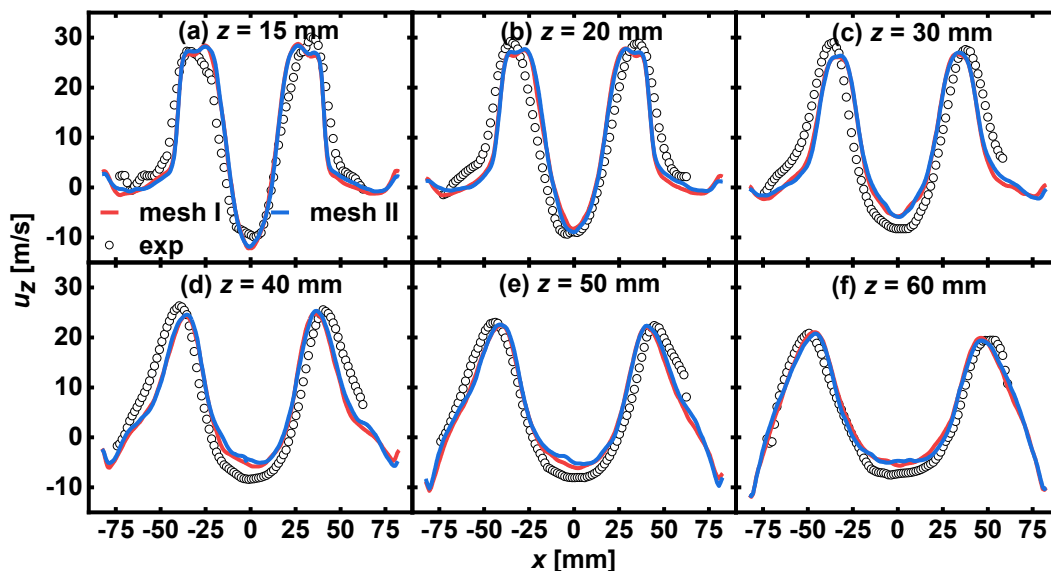


Fig. 4. Radial profiles of mean axial velocity at different streamwise locations in nonreacting flow, (a) $z = 15$ mm, (b) $z = 20$ mm, (c) $z = 30$ mm, (d) $z = 40$ mm, (e) $z = 50$ mm, (f) $z = 60$ mm. Circle: experiment data, red solid line: mesh I, blue solid line: mesh II.

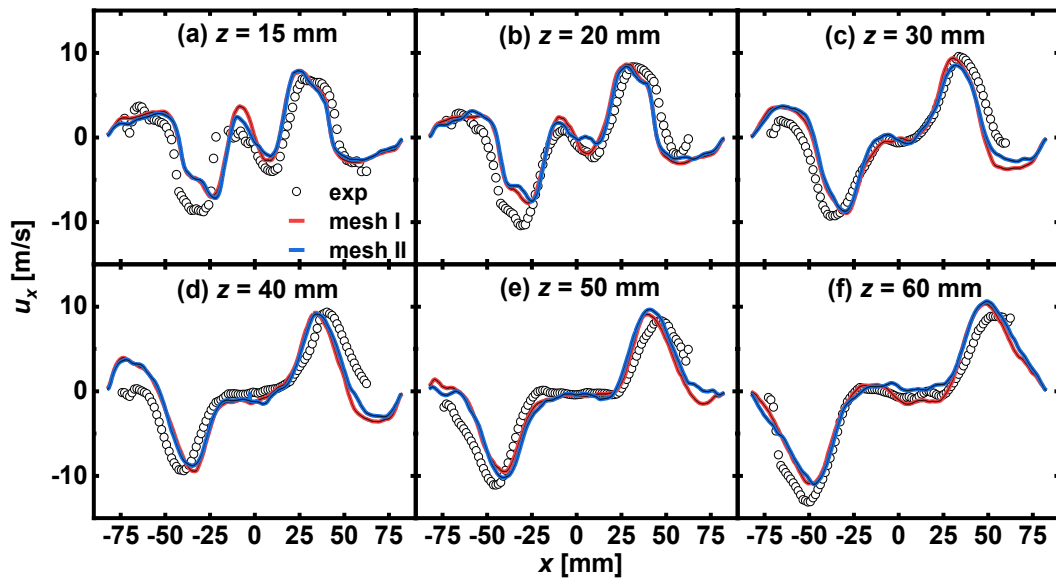


Fig. 5. Radial profiles of mean radial velocity at different streamwise locations in nonreacting flow, (a) $z = 15$ mm, (b) $z = 20$ mm, (c) $z = 30$ mm, (d) $z = 40$ mm, (e) $z = 50$ mm, (f) $z = 60$ mm. Circle: experiment data, red solid line: mesh I, blue solid line: mesh II.

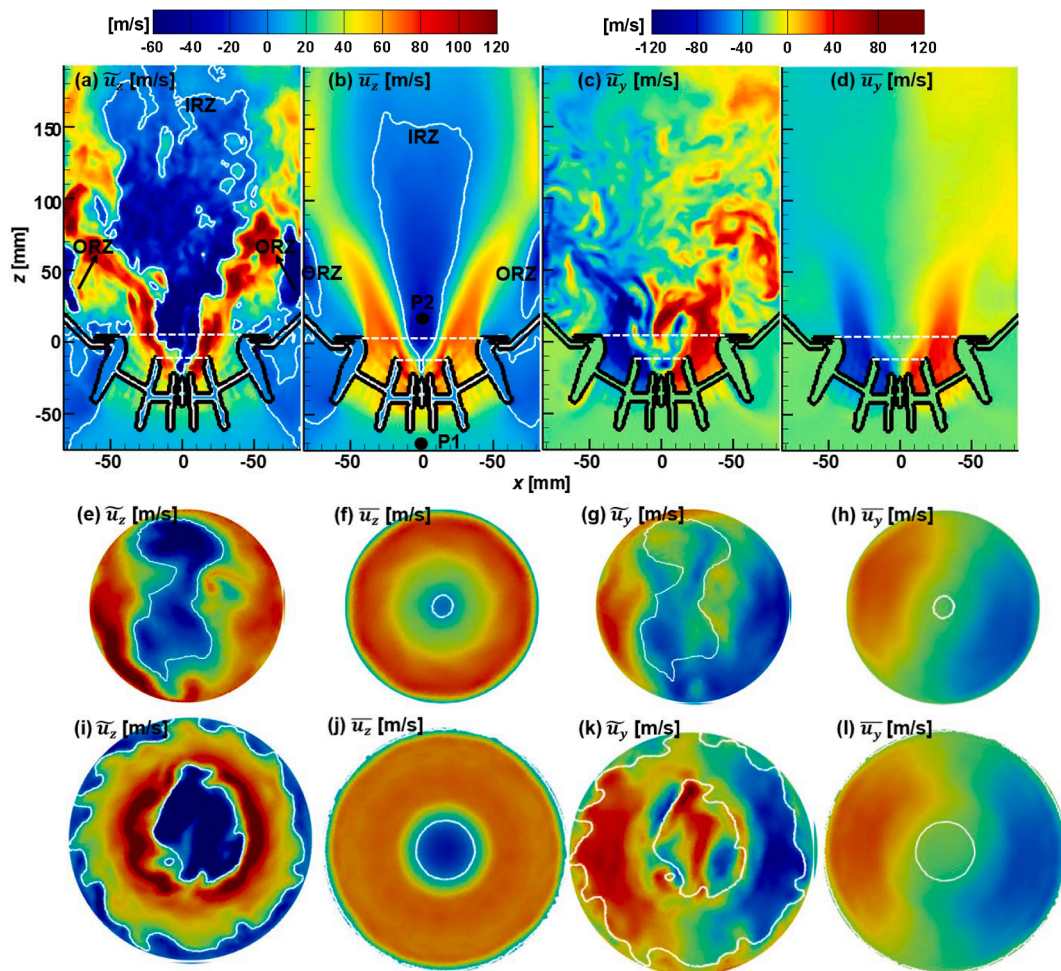


Fig. 6. (a) Resolved axial velocity (\tilde{u}_z), (b) averaged axial velocity (\bar{u}_z), (c) resolved swirl velocity (\tilde{u}_y), and (d) averaged swirl velocity (\bar{u}_y) at $z = 0$ mm, (e) – (h) \tilde{u}_z , \bar{u}_z , \tilde{u}_y and \bar{u}_y at the first main stage outlet, (i) – (l) \tilde{u}_z , \bar{u}_z , \tilde{u}_y and \bar{u}_y at the second main stage outlet. White solid line: zero axial velocity. Results from case 1.

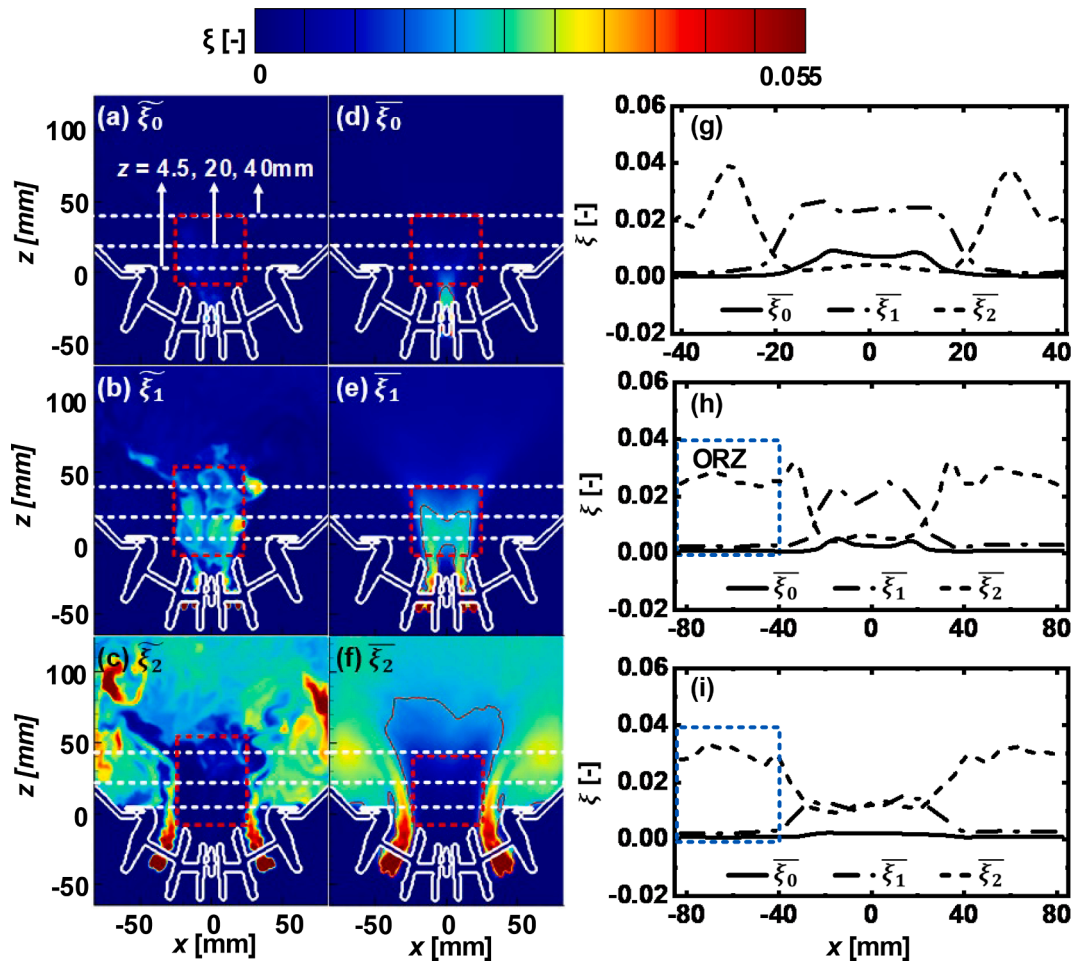


Fig. 7. (a) – (c) Resolved mixture fraction of the pilot stage ($\tilde{\xi}_0$), the first stage ($\tilde{\xi}_1$) and the second stage ($\tilde{\xi}_2$), (d) – (f) averaged mixture fraction of the pilot stage ($\bar{\xi}_0$), the first stage ($\bar{\xi}_1$) and the second stage ($\bar{\xi}_2$), (g) – (i) radial profiles of averaged mixture fraction along x – direction at $z = 4.5, 20$ and 40 mm. White dashed line: $z = 4.5, 20$ and 40 mm. Red solid lines are the isoline of $\xi = 0.02$. Results from case 1.

effects of the fuel ratio of first and second main stages and different ratios, R_ϕ , are considered in Table 3.

For the air inlet, the temperature, pressure, and velocity are 600 K, 100,000 Pa and 10.75 m/s, respectively. Uniform velocity with specified turbulent fluctuations (2%), zero-gradient pressure, and zero mixture fraction are enforced for the air inlet. For the fuel inlet, the CH_4 mass fraction and temperature are 1.0 and 300 K respectively. The fuel is injected into the domain normal to the fuel inlet, and the velocities in different stages are summarized in Table 4, which are estimated based on Table 3. No inlet turbulence is considered for the fuel streams. Total pressure condition is enforced for the pressure at the outlet, whereas the zero-gradient condition is for the rest variables. The walls are assumed to be non-slip and adiabatic.

4.3. Mesh sensitivity analysis

Two meshes (termed as mesh I and II hereafter) are generated to evaluate the sensitivity of the LES results to the CFD mesh resolution. The cell distributions in the combustor and over the swirler surface from mesh I are shown in Fig. 3. Note that the minimum and maximum cell sizes are the same in two meshes, which are 0.08 and 5 mm, respectively. For the swirler and flame regions, the cells are refined to 1 and 0.8 mm in mesh I and II respectively, to capture the detailed flow and flame structures. In both meshes, the cells become coarser further in the upstream plenum and downstream of the combustor. The total cell number is 6.76 and 12.29 million in mesh I and II, respectively.

Moreover, based on our *posterior* examination of the simulation results, y^+ of mesh I and II is lower than 9.6 and 8.9 at the combustor walls, respectively.

Here we validate our numerical method and solver based on non-reacting flow experimental data, i.e., case 0, measured in Harbin Engineering University. The velocity components in the non-reacting flow were measured by particle image velocimeter (PIV) made by TSI Inc. The PIV system include a double-pulsed Nd: YAG laser (New Wave Inc), a CCD camera (PowerView 4MP) and a synchronizer. The laser has a wavelength at 527 nm and frequency at 15 Hz. The pixel resolution of camera is 1600×1200 . TiO_2 seed particles mix the air before entering the combustor, which make the flow field visible. Vector fields were computed from particle image spatial cross correlations using the INSIGHT 3G software. In experiment, the straight section is used instead of the chamfer in the corner of the combustion chamber. Meanwhile, the cooling holes are also simplified. In this case, only air is injected with a mass flow rate of 0.15 kg/s, and the temperature and pressure are 300 K and 1 atm, respectively.

Figs. 4 and 5 compare the distributions of mean axial and radial velocities along the x -direction. In general, the axial velocities captured by the LES are well consistent with the experimental data. The locations of the shear layers and the magnitude of the maxima and minima are predicted accurately at different axial locations. The peaks of the mean axial velocity correspond to the shear layer, which decrease from 28 m/s at $z = 15$ mm to 22 m/s at $z = 60$ mm. Moreover, the negative axial velocities indicate existence of a recirculation zone. The increase in the

x-direction size of this zone implies that the recirculation zone gradually expands from $z = 15$ to 60 mm. Likewise, Fig. 6 shows the profiles of mean radial velocity at the same locations. Overall, the mean axial and radial velocities can be accurately captured with our LES. The LES-PaSR model is also validated in our previous work [40]. As shown in Figs. 4 – 5, the predicted velocities are almost the same using mesh I and II. In the following analysis, mesh I is used.

5. Results and discussion

5.1. Velocity and mixing fields in reacting flow (case 1)

Fig. 6 shows the contours of resolved and time averaged velocities in case 1. Note that Fig. 6(e)–6(h) and 6(i)–6(l) are the velocities at the first and second stage outlet. Immediately downstream of the swirlers, highly rotating flows can be observed, featured by large axial and swirl velocities. A long inner recirculation zone (IRZ) is generated in Fig. 6(a)–6(b), which starts downstream of the pilot stage. The width of the IRZ increases gradually along the flow direction, leading to a triangular structure. Based on the average axial velocity distribution in Fig. 6(b), the maximum of the length and width of the IRZ are approximately 249.8 and 71.3 mm, respectively. In addition, the outer recirculation zone (ORZ) is formed due to the confinement of the combustion chamber wall. The multi-stage fuel injection in this combustor is applied, and the swirl number of the first main stage (0.7) is lower than that of the second main stage (0.83), and hence the filtered and average swirl velocities, \bar{u}_y and \bar{u}_z , are generally lower than those from the second stage, as can be found in Fig. 6(c) and 6(d). The dark red region in Fig. 6(e) and 6(f) is due to contraction of the outlet of the first main stage, which pronouncedly increases the axial velocity. The distributions of \bar{u}_y and \bar{u}_z are similar at the downstream of the pilot stage and the first main stage, as illustrated in Fig. 6(g)–6(h) and Fig. 6(k)–6(l). This implies that the swirling flows from the second main stage dominate the aerodynamics in the combustor.

Fig. 7 shows the resolved and time averaged mixture fraction in case 1. The distributions of mixture fraction from the pilot, first and second stages in the combustor is shown separately. Since the fuel mass flow rate of the pilot stage accounts for <2% of the total fuel mass flow rate, the mixture fraction of the pilot stage is <0.01 in Fig. 7(a). The fuel of the pilot stage is mainly located in the red box (at -25 mm < x < 25 mm and z < 40 mm) in Fig. 7(a). After the fuel leaves the exit of the first stage swirler, it moves in the axial direction and no radial expansion is observed at z < 40 mm in Fig. 7(b). Moreover, at 40 mm < z < 100 mm, the fuel expands to the whole combustor. The first-stage fuel is mainly located near the IRZ, and a very small amount of them can be observed in the ORZ. In Fig. 7(c), the second-stage fuel rapidly transports to the ORZ subject to the swirling flows, and the high-concentration region is located at 50 mm < z < 80 mm. The red pockets in Fig. 7(c) indicate the localized rich area, e.g., caused by imperfect mixing. There is no discernable second-stage fuel in the red box (at -25 mm < x < 25 mm and z < 55 mm) in Fig. 7(c). Combining the analysis of Fig. 7(a)–7(b), one can conclude that the fuels in the red box are from the first (mainly) and pilot stages.

Fig. 7(d)–7(f) are the corresponding time-averaged mixture fraction. Considering that the values of the mixture fraction at three stages are quite different, the isoline of $\xi = 0.02$ is selected for clear illustrations. As shown in Fig. 7(d), the high-concentration pilot stage fuel is mainly located between the pilot stage exit ($z = -21.5$ mm) and the first stage exit ($z = -10.5$ mm), with V-shaped distribution in the red box. In Fig. 7(e), the first-stage fuel exhibits V-shaped distribution in the combustor, and most of the fuel is located at -25 mm < x < 25 mm and z < 30 mm. Moreover, most of the second-stage fuel is beyond the isoline of $\xi = 0.02$ in Fig. 7(f).

Fig. 7(e)–7(i) are the radial profiles of averaged mixture fraction along x - direction at $z = 4.5$, 20 and 40 mm. As shown in Fig. 7(g), a

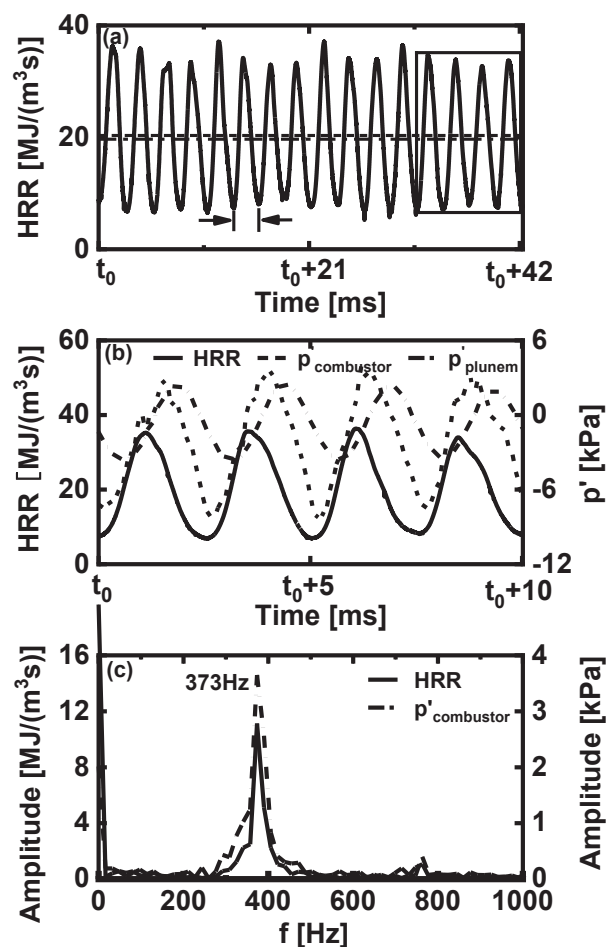


Fig. 8. (a) Time series of volume averaged HRR, (b) oscillations of HRR and pressure from the upstream plenum and combustor, and (c) signal spectra by fast-Fourier transform. Black dashed line in Fig. (a) is 20.32 MJ/(m³s), calculated from the product of fuel lower heating value and mass flow rate. Red dashed line in Fig. (a) is 19.66 MJ/(m³s), calculated from the average of the resolved HRR. Results from case 1.

very small amount of the pilot stage fuel exists at $z = 4.5$ mm (i.e., the exit of the second stage swirler). The peak of the first-stage fuel lies at $x = \pm 11.45$ mm with maximum value of 0.0274. The peak of the second-stage fuel is located at $x = \pm 30$ mm with maximum value of 0.0389. The mixture fraction from the second stage is zero at -20 mm < x < 20 mm, which is consistent with the finding in Fig. 7(g). The variations of the mixture fraction at each stage are generally similar in Fig. 7(h) and 7(i). As the fuel is transported downstream and has efficient mixing with the air, the mixture fraction peak value is decreased along the x - direction. As shown in the blue box in Fig. 7(h) and 7(i), only the second stage fuel exists in the ORZ, $\bar{\xi}_2$ in the ORZ at $z = 20$ mm is slightly lower than that at $z = 40$ mm.

5.2. Flame instability

Fig. 8(a) shows the time history of the resolved HRR in case 1, and the HRR is calculated by the volume averaging of the resolved HRR in the whole computational domain. The theoretical (based on the lower heating value) and average values of the HRR are 20.32 MJ/(m³s) and 19.66 MJ/(m³s), respectively. The incomplete combustion in the combustor makes the average HRR slightly less than the theoretical value. One can see that the HRR fluctuates periodically with time, and the average period is about 2.62 ms. The time series of the pressure in the air plenum and combustor and the averaged HRR fluctuations are

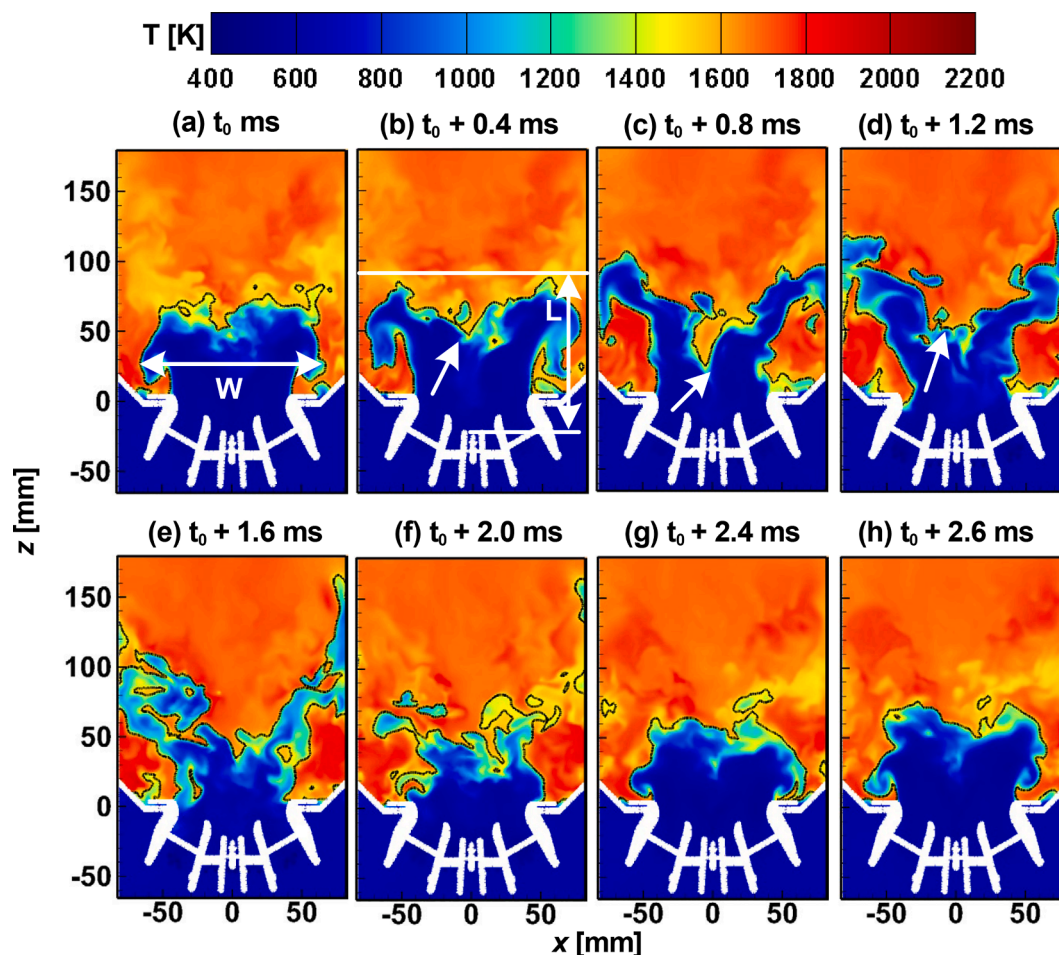


Fig. 9. Distributions of resolved temperature at different instants. Solid line: iso-line of $T = 1,500$ K. Image size: $165 \text{ mm} \times 245 \text{ mm}$. Results from case 1.

shown in Fig. 8(b). The two pressures are probed from the locations, P1 and P2, as marked in Fig. 6(a). These two probes are from the upstream plenum and combustion chamber. The pressure fluctuations share the same period as that of the HRR oscillations, but the phase difference of the upstream plenum and combustor pressure fluctuations is 23.3° . The phase difference of the HRR fluctuations and combustor pressure fluctuations is 46.1° , the phase difference is within the $\pi/2$ limit, which satisfies the Rayleigh criterion[41]. In addition, the constant amplitudes of the HRR and pressure indicate that the instability has reached the limit period oscillation. The signal spectra of the HRR and pressure are computed by fast-Fourier transform, and the results are characterized by a peak at approximately 373 Hz in Fig. 8(c). The maximum amplitude of the combustor pressure fluctuation and HRR are approximately 13.28 kPa and $31.9 \text{ MJ}/(\text{m}^3\text{s})$, respectively.

These amplitudes may be much smaller at higher operating pressure.

In the following, we will discuss the evolutions of the flame morphology within one HRR oscillation period as marked by the arrows in Fig. 8(a). Figs. 9-10 demonstrate the distributions of the resolved temperature and HRR at different instants within that period. The flame front is extracted from the isolines of $T = 1,500$ K. The width (W) of the flame envelope is the distance between the maximum and minimum locations in the x -direction, whilst the flame length (L) is the distance between the maximum location in the z -direction and the pilot stage exit. Fig. 11 shows the evolutions of the flame length L within one HRR oscillation period.

At t_0 ms, i.e., the beginning of a HRR oscillation period, the flame is relatively compact, attached to the burner exit. Both flame length and HRR are the smallest. Then both flame length and width increases, and the flame becomes V-shaped at $t_0 + 0.4$ ms, which is even more

pronounced at later instants in Fig. 9(c) and 9(d). Meanwhile, higher HRR can be observed along the flame front in Fig. 10(b). Due to the IRZ effects, more fresh gas is ignited in the region marked by the white arrow, and hence the central flame propagates upstream at $t_0 + 0.8$ ms. Due to the significant flame expansion in both longitudinal and radial directions, the flame or hot gas directly interacts with the chamber wall. This may remarkably increase the heat exchange between the gas and chamber walls, leading to the localized thermal load variations. Moreover, there is increased degree of local flame extinctions in the IRZ, see the arrow in Fig. 9(d) at $t_0 + 1.2$ ms. The flame length continues to increase from t_0 to $t_0 + 1.6$ ms, with relatively strong heat release for these instants.

The HRR and flame length peak at around $t_0 + 1.6$ ms. After $t_0 + 1.6$ ms, the flame length, width and HRR gradually decrease, which characterize the second half period. It is worth noting that there is a rapid decrease of flame length between $t_0 + 1.6$ and $t_0 + 1.8$ ms as revealed in Fig. 11. The flame length decreases from $0.438 L_c$ to $0.28 L_c$. During these rapid transition, the flames are broken and some isolated flamelets can be observed, which are not connected to the whole flame. However, the flame length is calculated from the flame root to the whole flame maximum in the z -direction, and these flamelets are not included. After $t_0 + 2.4$ ms, the flame becomes compact again and attached to the burner exit, like the results at t_0 ms. A new HRR oscillation period starts.

Fig. 12 demonstrates the oscillations of the pressure, axial velocity, and HRR in case 1. Specifically, Fig. 12(a)-12(b) show the pressure variations at the flame regime and upstream plenum, respectively. Note that t is one period of pressure oscillation, and t_1 is the time for pressure oscillation in the combustor propagating upstream into the plenum. The pressure oscillation of the plenum in Fig. 12(b) would also lead to

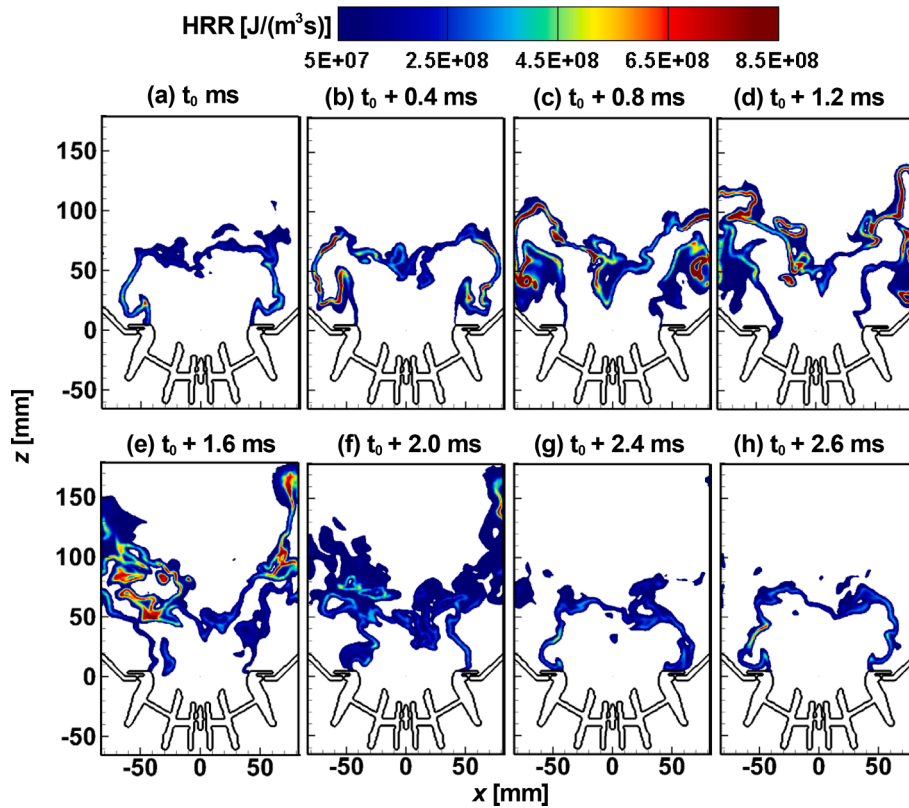


Fig. 10. Distributions of resolved heat release rate at different instants. Image size: 165 mm × 245 mm. Results from case 1.

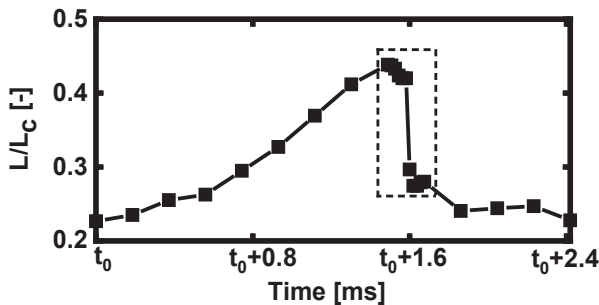


Fig. 11. Evolution of flame length within one HRR oscillation period. L_c is the streamwise distance between the second main stage outlet and the combustor outlet. Results from case 1.

velocity oscillation in Fig. 12(c). t_2 is the time delay between the velocity and pressure in the plenum, whilst t_3 is the time for the velocity oscillation in the plenum spreading downstream to the flame in Fig. 12(c).

As shown in Fig. 12(d), the velocity oscillations in the combustor are accompanied by secondary high-frequency fluctuations, due to wrinkled flames and high turbulence intensity. The response of the HRR is slightly delayed due to the mixing of reactant and chemical reactions. Therefore, t_4 is deemed the reaction delay time. t, t_1, t_2, t_3 and t_4 are about 2.61, 0.38, 0.68, 0.547 and 0.796 ms, respectively. The time between the HRR oscillation and pressure oscillation is sum of $t_1 - t_4$ and about 2.4 ms, which is consistent with the analysis in Fig. 8(b). The pressure oscillation would propagate upstream and downstream and cause the velocity oscillation, and the velocity oscillation will further affect the HRR. The HRR oscillation also in turn affects the pressure oscillation.

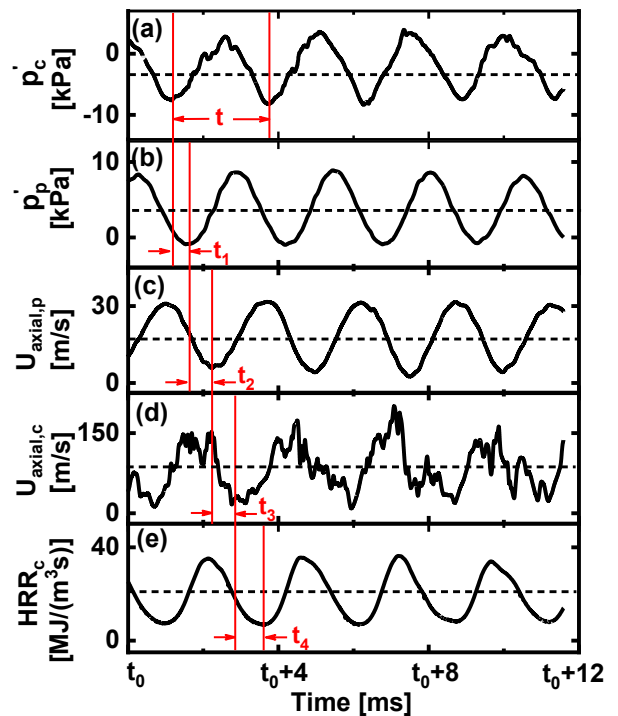


Fig. 12. (a) Time series of pressure in the combustor, (b) pressure in the plenum, (c) axial velocity in the plenum, (d) axial velocity in the combustor, and (e) heat release rate in the combustor. The subscripts c and p denote the variables for the combustor and plenum. The data in Figs. (a) - (d) are from the monitor points P1 and P2 in Fig. 6(b), HRR in Fig. (e) is the average of the resolved HRR in the whole combustor. Results from case 1.

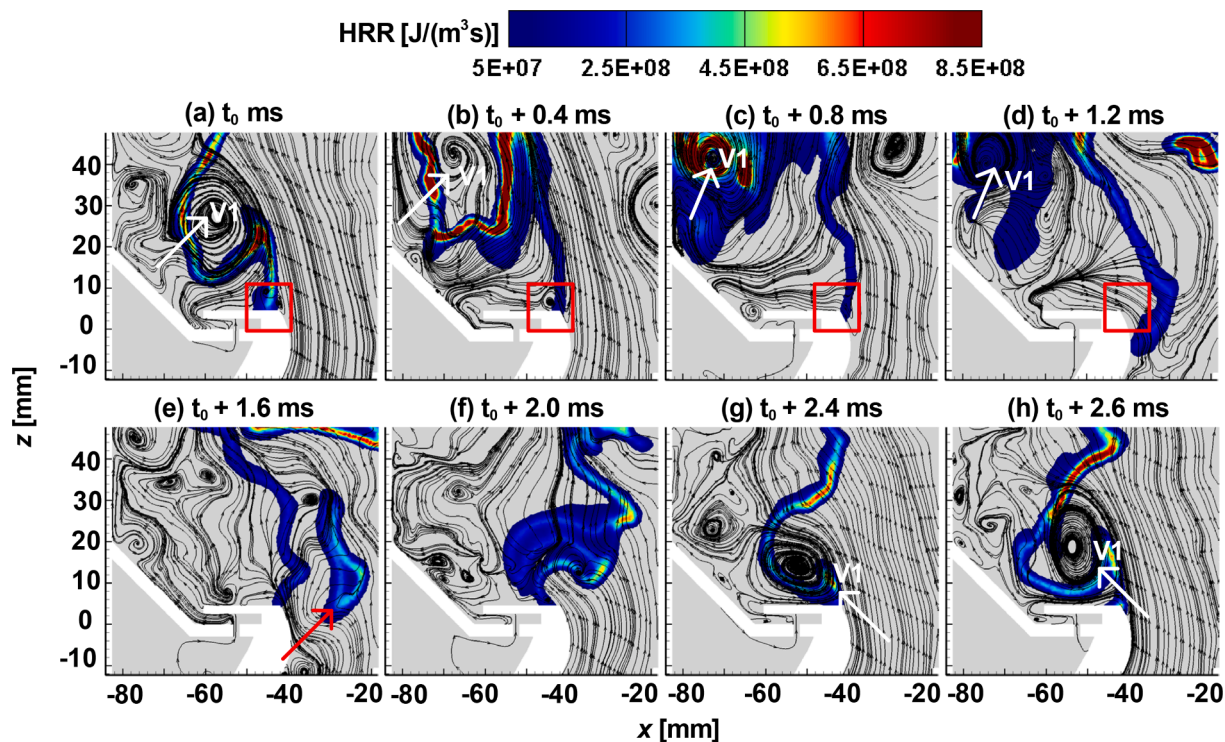


Fig. 13. Distributions of resolved HRR and streamlines near the flame root. Image size: 66 mm \times 60 mm. Results from case 1.

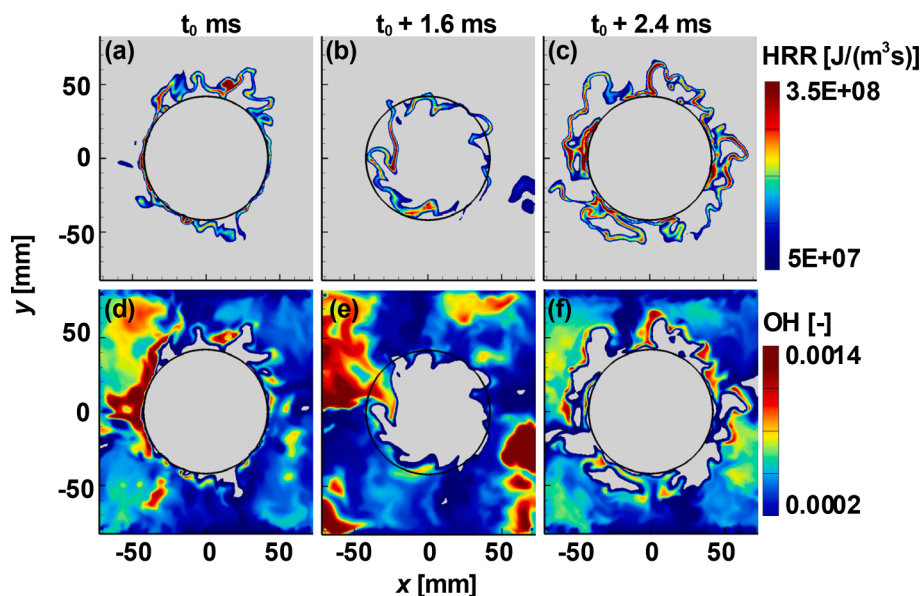


Fig. 14. Distributions of resolved HRR and OH mass fraction at $z = 10$ mm plane. Image size: 144 mm \times 166 mm. Results from case 1.

5.3. Flame root dynamics

Fig. 13 show the distributions of the resolved HRR at the flame root in one HRR oscillation period. At t_0 ms, the fluid in the ORZ is entrained by the vortex V1 at the flame root, and then V1 moves downstream at $t_0 + 0.4$ ms. Subsequently, a small amount of the fluid in the ORZ flows into the second stage, and therefore the small vortices at the swirler exit at t_0 and $t_0 + 0.8$ ms vanish, as indicated by the red frame in Fig. 13. At $t_0 + 1.2$ ms, the flame root moves towards the second stage with a large amount of fluid in the ORZ, and its HRR near the flame root is generally lower than the other sections of the flame front. At $t_0 + 1.6$ ms, the fresh gas pushes the flame roots downstream again, and an isolated island that

is not connected to the whole flame appears (see the red arrow in Fig. 13e). After $t_0 + 2.4$ ms, the vortex V1 appears again, and the flame root moves towards the ORZ as well.

Fig. 14 shows the distributions of the resolved HRR and OH mass fraction at $z = 10$ mm plane. The radius of black reference line is 42 mm, equal to the radius of the second stage exit. The HRR and high OH mass fractions are mainly concentrated on the reference line at t_0 ms. Then the flame root shrinks inwards at $t_0 + 1.6$ ms. A small amount of HRR and OH is on the surface of the reference line, and most of the HRR and OH is on the outside of the reference line at $t_0 + 2.4$ ms.

As shown in Fig. 15, the flame root changes with time periodically. It should be noted that the flame root location is extracted based on the

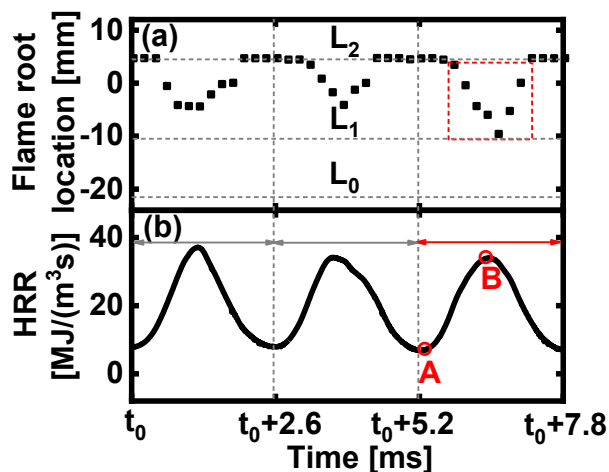


Fig. 15. Time series of (a) flame root location and (b) heat release rate. $L_0 - L_2$ are the exit locations of the pilot, first and second stages, respectively. Results from case 1.

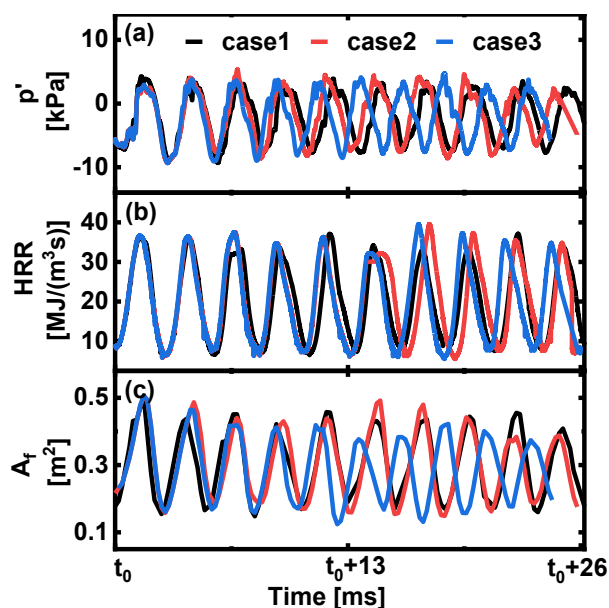


Fig. 16. Time series of (a) pressure fluctuation, (b) heat release rate, and (c) flame surface area. Pressure results are from the probe P2 marked in Fig. 6(b). The flame surface is defined as the *iso*-surface of $HRR = 100 \text{ MJ/m}^3/\text{s}$. Case 1: the fuel injected from all stages, i.e., pilot stage, first and second main stages; case 2: the pilot fuel switched off; case 3: both first main and pilot fuel switched off.

three-dimensional *iso*-surface of $T = 1500 \text{ K}$ in the domain. The period marked by the red arrows is the same cycle as discussed in Figs. 9–11. Some of the flame roots are located around the exit of the second stage, and the data in the red box mainly exist between the exits of the pilot and first stages, which indicates that the flashback happens only in the second main stage. Due to the data obtained from the three-dimension, the flashback at the flame root may be not shown in $y = 0 \text{ mm}$ plane, but the flame at these times is similar to that in Fig. 13(d).

The minima and maxima of the instantaneous flame root location in Fig. 15(a) are opposite to those of the HRR shown in Fig. 15(b). Specifically, the HRR is relatively small at the beginning of a period, and the flame root lies at the exit of the second stage swirler. As the HRR increases, the chemical reactions become intense and the mixing is stronger, which make the flame root move upstream. Subsequently, due

to decreased HRR, the flame root starts to move downstream and eventually returns to the swirler exit. In general, the fluctuations of the HRR affect the reaction intensity and mixing therefore the flame root location.

5.4. Effects of fuel mass flow rate from each stage

Up to this point, only case 1 has been discussed, in which the fuel is injected from all stages, i.e., pilot stage, first and second main stages (see their configuration in Fig. 2). The effects of different fuel mass flow rates from each stage will be studied in this section through cases 1–3 (their mass flow rates are shown in Table 3). To re-iterate, in case 2, the pilot fuel is switched off, whereas in case 3 both first main and pilot fuel is off. Note that the three simulations start with an identical initial field.

Fig. 16 shows the time series of pressure fluctuations (p'), HRR, and flame surface area (A_f) in cases 1–3. The data is calculated from the probe P2 marked in Fig. 6(b). As shown in Fig. 16(a), the initial three cycles are very close. Nonetheless, the periods become appreciably different after that, indicating that different oscillations appear in the combustor. In Fig. 16(b), in case 3 without pilot fuel and first main fuel supply, the amplitudes of the HRR have no significant changes. Moreover, the difference in the HRR periods is not as obvious as that in the pressure fluctuations. It is worth noting that the period of pressure fluctuation is smaller than that of HRR fluctuation, and the phase difference exists between them. The phase differences are 46.1° , 9.2° and 24.2° in case 1–3, respectively. This is because HRR fluctuations are correlated to the pressure fluctuations, it needs finitely long duration to respond to the pressure changes, and their detailed relations will be discussed later. The phase differences are within the $\pi/2$ limit in all cases, satisfying the Rayleigh criterion [39].

Fig. 16(c) shows the time sequence of the flame surface area. One can see the periodic change of the flame surface area when combustion instability occurs. The oscillation frequency and magnitude in case 1 is close to those of case 2, indicating that there is no significant influence from the pilot fuel. This is because the mass flow rate of the air and fuel on the pilot stage is $<2\%$ of the total air and fuel flow rates. Moreover, in case 3, all the fuels are injected from the second stage, and less fuel would penetrate the upstream of the IRZ, and therefore the flame surface area decreases.

Fig. 17 compiles the instantaneous locations of the central flame root (CFR) in cases 1–3. CFR is extracted from the isolines of $T = 1,500 \text{ K}$ in a cylindrical domain, defined by $\sqrt{x^2 + y^2} < 20 \text{ mm}$. The data points are colored by the streamwise coordinate, and the value of 4.5 mm in the color bar is the outlet of the second stage, i.e., L_2 in Fig. 2(b). The purple points mean that the CFR is below the burner exit (i.e., L_2) and the flashback happens in the second stage. No purple points exist in Fig. 17(a)–17(b), which indicates that no instantaneous flashback happens in cases 1 and 2. Most of the points are green and yellow, whilst limited points are orange and no points are purple in Fig. 17(a). This means that no flashback happens in case 1 and for most of the time the CFR are located between 15 and 55 mm (i.e., 10.5–50.5 mm off the burner exit). The CFR of case 2 is basically similar to that of case 1, but less CFR in case 2 locate further downstream, i.e., blue points in Fig. 17(b). Nonetheless, flashback happens, evidenced by the increased purple points in case 3 in Fig. 17(c). Overall, we can know from the above analysis that: (1) when the pilot stage is deactivated, the CFR is less affected; (2) when both pilot stage and first main stage are off, flame flashback will be more likely to happen.

The effects of fuel ratio of the first and second main stages on the flame unsteadiness will be also discussed. The inputs in cases 1 and 4 are compared and their details are tabulated in Table 3. The fuel ratio of the first and second main stages are 1:5.7 and 1:1 for cases 1 and 4, respectively. Fig. 18 shows the time series of HRR, pressure fluctuation, and flame surface area. Apparently, all of them change periodically. The amplitudes of HRR in case 4 are higher than that in case 1. Compared to

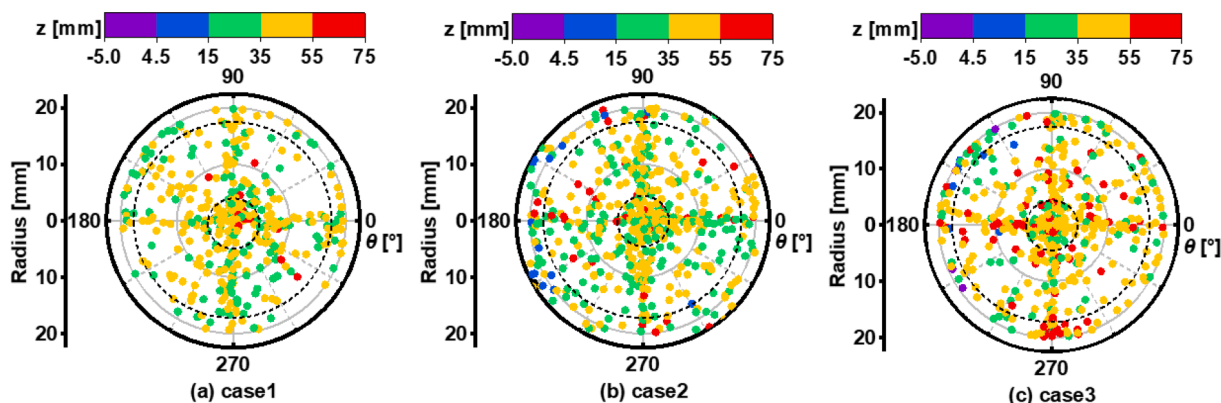


Fig. 17. Locations of central flame root in (a) case 1, (b) 2, and (c) 3. The black dashed lines ($R = 5.65$ and 17.5 mm) are the radii of the exits of the pilot and first stages. Case 1: the fuel injected from all stages, i.e., pilot stage, first and second main stages; case 2: the pilot fuel switched off; case 3: both first main and pilot fuel switched off.

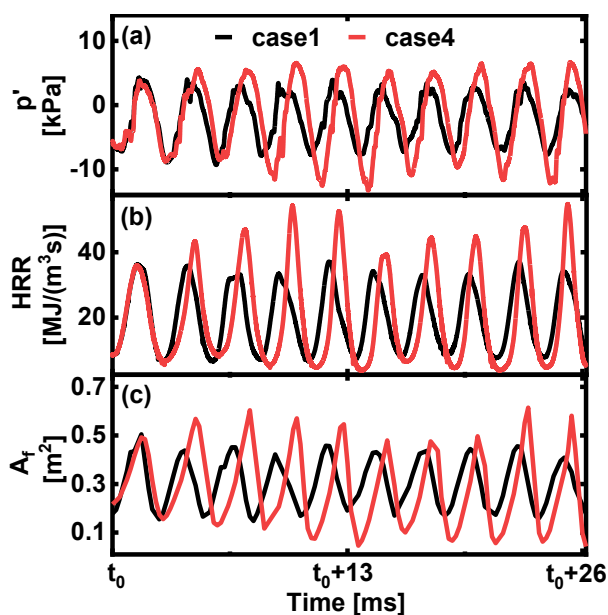


Fig. 18. Time series of (a) pressure fluctuation, (b) heat release rate, and (c) flame surface area in case 1 and 4. Pressure results are from the probe P2 marked in Fig. 6(b). The flame surface is the iso-surface of $HRR = 100$ MJ/m³/s. The fuel ratio of the first and second main stages are 1:5.7 and 1:1 in cases 1 and 4, respectively.

case 1, change of the flame surface area in case 4 are larger, with the maximum and minimum being 0.61426 and 0.04272 m², respectively. This is mainly caused by the different global equivalence ratios of each stage. Specifically, the equivalence ratio in the first and second main stage are 0.54 (hence globally fuel lean) in case 1. The fuel flow rate ratio of the first and second main stages is 1:1 in case 4, which means that the equivalence ratio of two stages is 1.83 and 0.31 , respectively, indicating globally fuel-rich composition from the first main stage and lean-rich from the second one. Fuel-rich composition in the first main stage may lead to flame flashback, which would lead to strong combustion unsteadiness. Therefore, the amplitudes of pressure fluctuation, HRR and flame surface area in case 4 are all higher than those in case 1.

The effects of fuel ratio of the first and second main stages on the location of central flame root are shown in Fig. 19. As discussed in Fig. 17, no flashback happens in case 1. However, it is different in case 4. The reader should be reminded that the value of -21.5 , -10.5 and 4.5 mm in the color bar in Fig. 19(b) correspond to the exit locations of the

pilot, first and second stages, i.e., $L_0 - L_2$ in Fig. 2(b). The green, orange, and red points indicate that the CFR is higher than the second main stage and no flashback happens. The light blue points are located between the exit of the first and second main stages, which means that the flashback happens in the second main stage. The dark blue and purple points with $R > I$, $I < R < II$ and $R > II$ mean that the CFR is in the pilot stage, first stage and second stage. From the above analysis, we can see that the equivalence ratio of the first main stage plays an important role in occurrence of the flame flashback.

The central flame root location and flame flashback are similar in cases 1–3, while they are quite different between cases 1 and 4. Therefore, the central flame root location and flame flashback in case 4 will be discussed. One oscillation period in case 4 is selected for analyzed, and the period is about 2.7 ms, and the flashback occurs at $t_0 + 1.2$ ms and ends at $t_0 + 2.2$ ms. Fig. 20 is the resolved temperature and streamlines in case 4, which can show the progress of flashback. There is no flashback at $t_0 + 0.6$ ms. As the high-temperature burned gas moves upstream, the vortex (V1) moves downstream, and a small amount of high-temperature burned gas (H1) is separated from V1 at $t_0 + 1.2$ ms. Therefore, the flashback happens in the second stage at this moment. V1 and V2 at $t_0 + 1.2$ ms are combined as V1 at $t_0 + 1.2$ ms, the downstream movement of V1 makes more hot gas into the second main stage. From $t_0 + 1.2$ ms to $t_0 + 1.8$ ms, H1 is gradually approaching the right side of the first main stage, and the flashback is more obvious. The flashback happens in the first and second stage from $t_0 + 1.4$ ms to $t_0 + 1.8$ ms. The flame is pushed downstream due to the increased velocity of the incoming air at $t_0 + 2.0$ ms. The flashback is relatively weakened and disappears at $t_0 + 2.0$ and $t_0 + 2.2$ ms, respectively. As discussed in this paragraph, the flashback is due to the flame propagation upstream. The flashback occurs when the flame propagation velocity is greater than that of fresh mixture, and the flame propagates upstream into the swirler. This can also explain why no flashback exists in case 1. Due to the effect of the fuel ratio of the first and second main stages, the HRR of case 1 is smaller than that of case 4 in Fig. 17(b), and the distance or ability of flame to propagate upstream of case 1 (as shown in Fig. 9) is much smaller than that of case 4. Therefore, flashback only happens in case 4.

6. Conclusions

The LES/PaSR model with a GRI 3.0 mechanism is used to simulate the flow field, vortex-mixing interaction, and flame dynamics in low emission tower-type coaxial-staged combustor. The fuel, methane, is injected from three stages, namely, the pilot stage, the first main stage and the second main stage. Radiation is not considered in the LES. The velocities solved by LES are in good agreement with the experimental data in non-reacting flows. The following conclusions can be obtained:

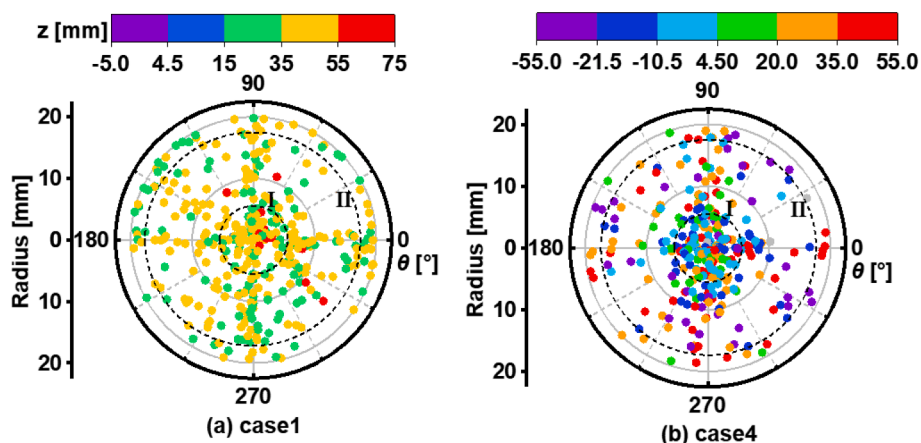


Fig. 19. Central flame root location: (a) case 1 and (b) case 4. Black dashed lines (I and II) indicate the radii of the exits of the pilot and first stages. The fuel ratio of the first and second main stages are 1:5.7 and 1:1 in cases 1 and 4, respectively.

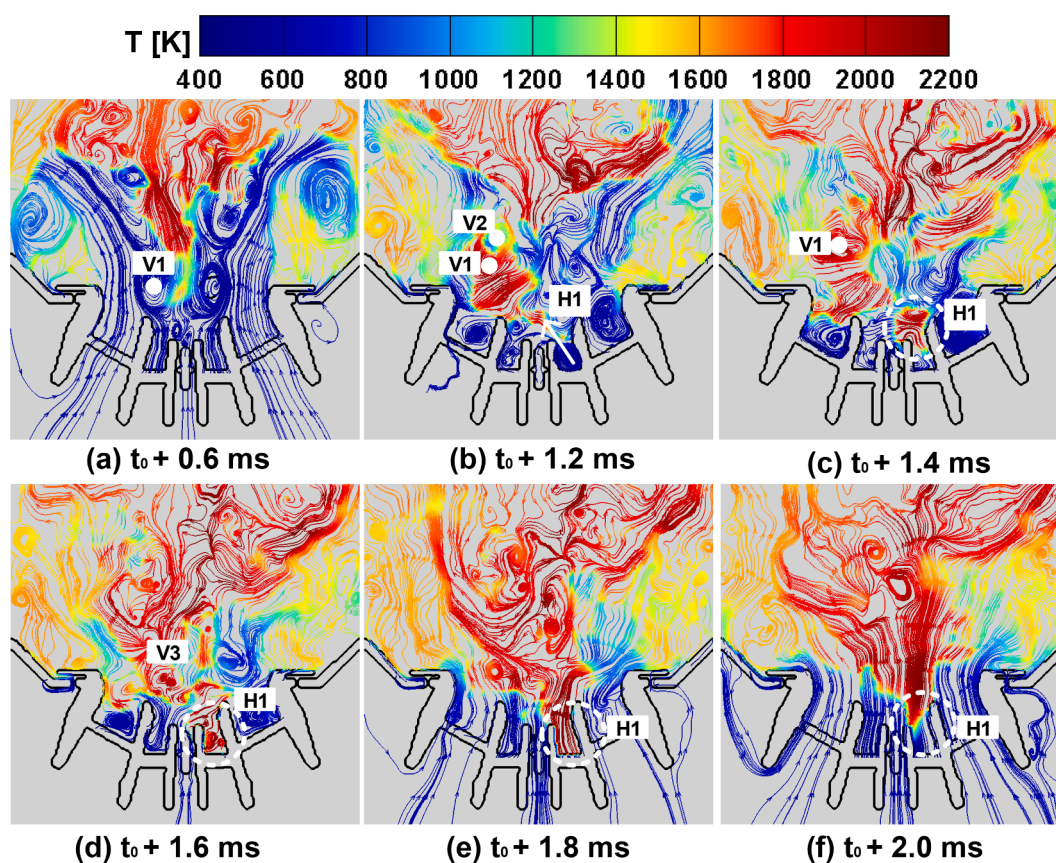


Fig. 20. Time sequence of the resolved temperature in case 4. The streamlines are colored by temperature.

- (1) The inner recirculation zone (IRZ) and the outer recirculation zone (ORZ) are formed in the combustor, and the maximum of the average length and width of the IRZ are approximately 249.8 and 71.3 mm. Based on the time averaged mixture fraction, the pilot-stage fuel exists at $-25 \text{ mm} < x < 25 \text{ mm}$ and $-21.5 \text{ mm} < z < 40 \text{ mm}$. The first-stage fuel exhibits a V-shaped distribution in the combustor. Most of the first-stage fuel is located at $-25 \text{ mm} < x < 25 \text{ mm}$ and $z < 30 \text{ mm}$. The second-stage fuel mainly exists in the ORZ and $z > 100 \text{ mm}$.
- (2) In case 1, the pressure and heat release rate in the combustor fluctuate periodically with a frequency of around 373 Hz. Both HRR and pressure fluctuations increase and then decrease with

- time, and there is a phase difference of 46.1° between them. The maximum amplitude of the combustor pressure fluctuations and HRR are approximately 13.28 kPa and $31.9 \text{ MJ}/(\text{m}^3\text{s})$, respectively. The flame shape changes periodically from attached flame, V-shaped flame, to attached flame in one HRR cycle. Moreover, the flame length increases first and then decreases with time. Furthermore, in case 1, vortex dynamics significantly change the behaviors of the flame root. The flame roots move upstream and then downstream when the heat release rate is relatively lower.
- (3) The pilot stage and first main stages are turned-off, to examine the effects of the fuels from various stages. It is found that the combustion instabilities occur in all cases. The heat release rate

fluctuations and the pressure fluctuations are in phase, and the dominant frequencies are 373 Hz, 402 Hz and 420 Hz, respectively. The central flame root moves upstream in cases 1–3. One also find that the effects of the fuel ratio of the first and second main stages have a significant influence on heat release rate fluctuations, pressure fluctuations, and the central flame root behaviors.

CRedit authorship contribution statement

Enhui Liu: Methodology, Software, Validation, Formal analysis, Writing – original draft, Writing – review & editing. **Jinghe Lu:** Methodology, Validation, Formal analysis. **Chenyang Cao:** Methodology, Software, Validation. **Xiao Liu:** Writing – review & editing, Resources, Funding acquisition, Supervision. **Hongtao Zheng:** Funding acquisition, Supervision. **Huangwei Zhang:** Conceptualization, Formal analysis, Resources, Project administration, Funding acquisition, Supervision.

Declaration of Competing Interest

The authors declare that they have no known competing financial interests or personal relationships that could have appeared to influence the work reported in this paper.

Data availability

Data will be made available on request.

Acknowledgement

The simulations are performed with the computational resources from National Supercomputing Center Singapore (NSCC, <https://www.nsc.sg/>). EL is supported by China Scholarship Council (CSC) and the National Science and Technology Major Project (2017-III-0006-0031), China. We thank Zhihao Zhang, Shengnan Li and Guangpu Lv in Harbin Engineering University for the PIV measurements.

References

- [1] C.M. Lee, C. Chang, S.Kramer, NASA project Develops Next Generation Low-emissions Combustor Technologies", AIAA Paper 2013-540.
- [2] International Civil Aviation Organization. International standards and recommended practices, environmental protection, Annex 16 , to the convention on international civil aviation, Volume II, aircraft engine emissions. Montreal: ICAO, 2017.
- [3] Lefebvre AH, Ballal BR. Gas turbine combustion. CRC Press; 1998.
- [4] Jaravel T, Riber E, Cuenot B, Bulat G. Large Eddy Simulation of an industrial gas turbine combustor using reduced chemistry with accurate pollutant prediction. *Proc Combust Inst* 2017;36(3):3817–25.
- [5] Shoji T, Tachibana S, Suzuki T, Nakazumi Y, Yokomori T. A new pattern of flame/flow dynamics for lean-premixed, low-swirl hydrogen turbulent jet flames under thermoacoustic instability. *Proc Combust Inst* 2021;38(2):2835–43.
- [6] Seo S, Lee S-Y. Effects of Unmixedness on Combustion Instabilities in a Lean-Premixed Gas Turbine Combustor. *Flow Turbul Combust* 2010;85(1):95–112.
- [7] Candel S. Combustion dynamics and control: Progress and challenges. *Proc Combust Inst* 2002;29(1):1–28.
- [8] Benim AC, Syed KJ. Flashback mechanisms in lean premixed gas turbine. San Diego: Academic Press; 2015.
- [9] Dhanuka SK, Temme JE, Driscoll JF, Mongia HC. Vortex-shedding and mixing layer effects on periodic flashback in a lean premixed prevaporized gas turbine combustor. *Proc Combust Inst* 2009;32(2):2901–8.
- [10] Won SH, Rock N, Lim SJ, Nates S, Carpenter D, Emerson B, et al. Preferential vaporization impacts on lean blow-out of liquid fueled combustors. *Combust Flame* 2019;205:295–304.
- [11] Stöhr M, Arndt CM, Meier W. Transient effects of fuel–air mixing in a partially-premixed turbulent swirl flame. *Proc Combust Inst* 2015;35(3):3327–35.
- [12] Stöhr M, Boxx I, Carter CD, Meier W. Experimental study of vortex-flame interaction in a gas turbine model combustor. *Combust Flame* 2012;159(8):2636–49.
- [13] Litvinov I, Yoon J, Noren C, Stöhr M, Boxx I, Geigle KP. Time-resolved study of mixing and reaction in an aero-engine model combustor at increased pressure. *Combust Flame* 2021;231:111474.
- [14] Chen ZX, Swaminathan N, Stöhr M, Meier W. Interaction between self-excited oscillations and fuel–air mixing in a dual swirl combustor. *Proc Combust Inst* 2019;37(2):2325–33.
- [15] Zhang Bo, Shahsavari M, Rao Z, Yang S, Wang B. Thermoacoustic instability drivers and mode transitions in a lean premixed methane-air combustor at various swirl intensities. *Proc Combust Inst* 2021;38(4):6115–24.
- [16] Meier W, Weigand P, Duan X, Giezendannerthoben R. Detailed characterization of the dynamics of thermoacoustic pulsations in a lean premixed swirl flame. *Combust Flame* 2007;150(1-2):2–26.
- [17] Fredrich D, Jones WP, Marquis AJ. Thermo-acoustic Instabilities in the PRECCINSTA Combustor Investigated Using a Compressible LES-pdf Approach. *Flow Turbul Combust* 2021;106(4):1399–415.
- [18] Temme JE, Allison PM, Driscoll JF. Combustion instability of a lean premixed prevaporized gas turbine combustor studied using phase-averaged PIV. *Combust Flame* 2014;161(4):958–70.
- [19] Wang X, Han M, Han X. Flame structures and thermoacoustic instabilities of centrally-staged swirl flames operating in different partially-premixed modes. *Energy* 2021;236:121512.
- [20] Chen ZX, Langella I, Swaminathan N, Stöhr M, Meier W, Kolla H. Large Eddy Simulation of a dual swirl gas turbine combustor: Flame/flow structures and stabilisation under thermoacoustically stable and unstable conditions. *Combust Flame* 2019;203:279–300.
- [21] Agostinelli PW, Laera D, Boxx I, Gicquel L, Poinso T. Impact of wall heat transfer in Large Eddy Simulation of flame dynamics in a swirled combustion chamber. *Combust Flame* 2021;234:111728.
- [22] Arndt CM, Severin M, Dem C, Stöhr M, Steinberg AM, Meier W. Experimental analysis of thermo-acoustic instabilities in a generic gas turbine combustor by phase-correlated piv, chemiluminescence, and laser raman scattering measurements. *Exp Fluids* 2015:56–9.
- [23] Poinso T, Veynante D. Theoretical and numerical combustion. R.T. Philadelphia, PA19118, USA: Edwards Inc; 2001. p. 162–3.
- [24] Nicoud F, Ducros F. Subgrid-Scale Stress Modelling Based on the Square of the Velocity Gradient Tensor. *Flow Turbul Combust* 1999;62:183–200.
- [25] Chomiak J. Combustion: A study in theory, fact and application. United states: Abacus Press/Gordon Breach; 1990.
- [26] Bulat G, Fedina E, Fureby C, Meier W, Stopper U. Reacting flow in an industrial gas turbine combustor: LES and experimental analysis. *Proc Combust Inst* 2015;35(3):3175–83.
- [27] Afarin Y, Tabejamaat S. *Combust Theory Model* 2013;17(3):383–410. <https://doi.org/10.1080/13647830.2012.742570>.
- [28] Fureby C. *J Eng Gas Turbines Power* 2012;134:041503.
- [29] Han X, Li J, Morgans AS. Prediction of combustion instability limit period oscillations by combining flame describing function simulations with a thermoacoustic network model. *Combust Flame* 2015;162:3632–47.
- [30] Chomiak J. Combustion a Study in Theory, Fact and Application. New York: Abacus Press/Gordon and Breach Science Publishers; 1990.
- [31] Huang Z-W, He G-Q, Qin F, Wei X-G. Large eddy simulation of flame structure and combustion mode in a hydrogen fueled supersonic combustor. *Int J Hydrog Energy* 2015;40(31):9815–24.
- [32] Palies P, Durox D, Schuller T, Candel S. The combined dynamics of swirler and turbulent premixed swirling flames. *Combust Flame* 2010;157(9):1698–717.
- [33] <https://cpp.openfoam.org/v6>.
- [34] G. Smith, D. Golden, M. Frenklach, N. Moriarty, et al. GRI 3.0 Mechanism, 1999, <http://www.me.berkeley.edu/gri_mech/>.
- [35] T. Holzmann, Mathematics, Numerics, Derivations and OpenFOAM, 2016.
- [36] Pope SB. Computationally efficient implementation of combustion chemistry using in situ adaptive tabulation. *Combust Theory Modelling* 1997;1:41–63.
- [37] Lu L, Pope SB. An improved algorithm for in situ adaptive tabulation. *J Comput Phys* 2009;228(2):361–86.
- [38] Liang L, Stevens JG, Raman S, Farrell JT. The use of dynamic adaptive chemistry in combustion simulation of gasoline surrogate fuels. *Combust Flame* 2009;156(7):1493–502.
- [39] Contino F, Lucchini T, D'Errico G, Duynslaegher C, Dias V, Jeanmart H. Simulations of advanced combustion modes using detailed chemistry combined with tabulation and mechanism reduction techniques. *SAE Int J Engines* 2012;5:185–96.
- [40] Liu X. Study on low emission combustion chamber design and premixed combustion characteristics. Harbin Engineering University; 2017.
- [41] Rayleigh L. The explanation of certain acoustical phenomena. *Roy Inst Proc* 1878; 8:536–42.